Geochemistry, Geophysics, Geosystems®

AGU ADVANCING EARTH AND SPACE SCIENCE

RESEARCH ARTICLE
10.1029/2021GC009990

New Paleointensity Data Suggest Possible Phanerozoic-Type Paleomagnetic Variations in the Precambrian

Simon J. Lloyd[1], Andrew J. Biggin[1], and Zheng-Xiang Li[2]

[1]Department of Earth, Ocean and Ecological Sciences, Geomagnetism Laboratory, University of Liverpool, Liverpool, UK, [2]Earth Dynamics Research Group, The Institute for Geoscience Research, School of Earth and Planetary Sciences, Curtin University, Bentley, WA, Australia

Key Points:

- New unexpected paleointensity data are obtained for key periods of the Precambrian which are in stark contrast to existing data
- Combined data now suggest high Precambrian field variability, similar to that observed in the Phanerozoic
- Implies that caution should be applied when using sparse data sets to infer or constrain key events in Earth history

Supporting Information:

Supporting Information may be found in the online version of this article.

Correspondence to:

S. J. Lloyd,
s.lloyd@liverpool.ac.uk

Citation:

Lloyd, S. J., Biggin, A. J., & Li, Z.-X. (2021). New paleointensity data suggest possible Phanerozoic-type paleomagnetic variations in the Precambrian. *Geochemistry, Geophysics, Geosystems*, *22*, e2021GC009990. https://doi.org/10.1029/2021GC009990

Received 21 JUN 2021
Accepted 28 SEP 2021

Abstract The state of the geomagnetic field throughout the Precambrian era is largely unknown. Approximately 8% of global paleointensity records account for ~4 billion years of Earth history. Despite this severe sparsity, the data are used to constrain models that predict the timing of significant deep earth events such as inner core nucleation. This carries with it the assumption that the Precambrian paleomagnetic field was less variable when compared to the Phanerozoic, or at least that the sparse data can be averaged to accurately represent a particular time period. This study reports new paleointensities from the West Australian Craton at 755 Ma (the Mundine Wells dyke swarm) and 1,070 Ma (the Bangemall Sills); both of which occurred within ~30 Ma from times at which extremely weak and anomalously strong fields, respectively, have been reported. Virtual dipole moments of 6.3 ± 0.1 Am$^2 \times 10^{22}$ and 1.8 ± 1.2 Am$^2 \times 10^{22}$ have been obtained from the two suites of mafic rock units which are substantially different to the previous measurements for the two respective ages. The findings suggest that field variability over tens of Myrs in the Precambrian was greater than has previously been assumed. This is supported by comparisons of paleosecular variation and distributions of virtual dipole moments. If variability in the Precambrian field is similar to that observed in the Phanerozoic, spatial or temporal anomalies may introduce significant bias to statistical analyses and model constraints, implying that caution should be employed in the interpretation of the Precambrian dipole moment records.

1. Introduction

Paleointensity has been used to either constrain or signify the onset of deep earth events such as the formation of the inner core (Biggin et al., 2015; Bono et al., 2019; Driscoll, 2016; Lloyd, Biggin, et al., 2021). An important requirement is that the data accurately represents the true paleofield. Systematic biases can affect the fidelity of specimen and site-level paleointensity results (Smirnov & Tarduno, 2005; Smirnov et al., 2017) and nonideal effects such as natural thermo-chemical and laboratory induced alteration, multi-domain carriers and other causes of Arai-slope curvature must be overcome (Biggin & Böhnel, 2003; Kosterov & Prévot, 1998; Shaar & Tauxe, 2015; Shcherbakov et al., 2019). Further complications exist when interpreting the data; for example, a fundamental assumption is made in long term statistical analyses, that the field is adequately defined for binned periods (Biggin et al., 2015; Kulakov et al., 2019). This requires that fluctuations occurring in both direction and intensity as a result of paleosecular variation are sufficiently represented by good data.

Evidence suggests that Earth's geomagnetic field has existed for ~3.5–4.0 Ga (Biggin et al., 2011; Tarduno et al., 2020); however, 90% of global paleointensity data is from the last 50 Ma. Therefore, understanding the long-term evolution of the geodynamo in the Precambrian, currently requires models which are either constrained by, or based on, limited data with gaps of up to hundreds of millions of years (PINT database v.2015.05; http://earth.liv.ac.uk/pint/; Biggin et al., 2015; Bono et al., 2019; Lloyd, Biggin, et al., 2021; Smirnov et al., 2017). Such sparse data may lead to the possibility of bias or aliasing, depending on whether long-term variations are reliably averaged out. For example, substantial periods of extreme variation in dipole stability are observed in the Phanerozoic between 65 and 200 Ma related to changes in the average polarity reversal rate (Kulakov et al., 2019).

Here we set out to determine whether long-term variations in field strength (tens to hundreds of Myrs) in the Precambrian are comparable to those observed in the Phanerozoic, and to gain a better appreciation of

whether existing models are accurately representing these long-term variations where a severe paucity of data exists. We target two important periods in the Precambrian era, approximal either to a large number (7) of weak-field observations which are linked to the onset of inner core nucleation (ICN) (720 Ma; Lloyd, Biggin, et al., 2021) or to the anomalously high intensities from the Mid-Continent Ridge (1,087 Ma; Kulakov et al., 2013; Sprain et al., 2018). Reported here are the first late Precambrian paleointensity data from the West Australian Craton: that of the Mundine Wells dyke swarm (755 ± 3 Ma) and the Bangemall Sills (1,070 ± 6 Ma). Both rock units were originally studied with the aim of better defining the apparent polar wander path for the Australian continent with respect to Laurentia during Precambrian supercontinent cycles (Wingate & Giddings, 2000: Wingate et al., 2002). The paleomagnetic poles obtained are considered robust for paleogeographic reconstruction (Li et al., 2008; Meert & Torsvik, 2003). Multiple lines of evidence for primary TRMs are reported from both localities, providing good potential for paleointensity investigation. These includes positive fold and baked-contact tests, low within-site dispersion, high unblocking temperatures of single-domain (SD) magnetite, and little reported alteration in high temperature-susceptibility experiments (Wingate & Giddings, 2000; Wingate et al., 2002).

The temporal proximity of these rock units to existing data allows for more accurate comparisons of Precambrian field characteristics and intensity variations to those observed in the Phanerozoic. A similar order of variability combined with a severe sparsity of data may introduce considerable bias to statistical analyses, and would suggest a more cautious approach when using such data to constrain key Earth events.

2. Background and Geological Setting

The Mundine Wells dyke swarm (MDS) and Bangemall Sills (BMS) are located close to one another in Western Australia (Figure 1a), with the former cross-cutting the latter in places. The extensive MDS intrude into Archean and Proterozoic rocks of the Pilbara Craton, trending mainly NNE. The dykes represent the last known igneous event in the region and are essentially undeformed, cutting vertically across all older rocks. The Bangemall Supergroup was deposited in the Edmund and Collier Basins of Western Australia during the Mesoproterozoic. The quartz dolerite BMS intrude into these clastic and carbonate sedimentary rocks, and are widely distributed across the basins. The sills are typically ~100 m thick and are generally conformable with the hosting strata.

2.1. Background—MDS

The dykes are typically ~30 m wide and consist of fine to medium grained quartz dolerites; plagioclase, interstitial quartz and quartz-feldspar is commonly contained in most samples, with orthopyroxene and clinopyroxene found less commonly (Wingate & Giddings, 2000). U-Pb dating put MDS emplacement at 755 ± 3 Ma (Wingate & Giddings, 2000). Alteration in the quartz dolerites is reported to be slight to moderate in places and is variable between dykes and between cores from the same dyke; plagioclase is locally sericitized, and pyroxenes may be partially altered.

Wingate and Giddings (2000) interpreted a low coercivity component as resulting from a lightning induced isothermal remanent magnetization (IRM) and noted that this was removed by an AF pre-treatment to 15 or 20 mT. The high coercivity remanence of most specimens are consistently oriented to NNE with shallow to moderate downwards inclination. Thermal demagnetization of one specimen from each of four dykes yielded similar directions with unblocking temperatures in the range 570–580°C. The dominant magnetic carrier is interpreted to be SD magnetite, which is supported by high-temperature susceptibility results which show well-defined Hopkinson peaks close to 580°C, indicative of the presence of SD magnetite (Schmidt, 1993).

Positive baked contact tests at sites A and C agree with positive results from a contact test at site E (Wingate & Giddings, 2000), where the dyke crosscuts an older Bangemall sill. Here, there is evidence of primary remanence based on agreement in direction between magnetizations in the dyke and the baked dolerite sill near the contact and a stable coherently directed remanence in the unbaked dolerite sill which is different in direction from that of the dyke.

A total of eight dykes were sampled in the current study, four of which were positively identified from the original study by drill holes. The remaining dykes were close to the original ones based on the description

10.1029/2021GC009990

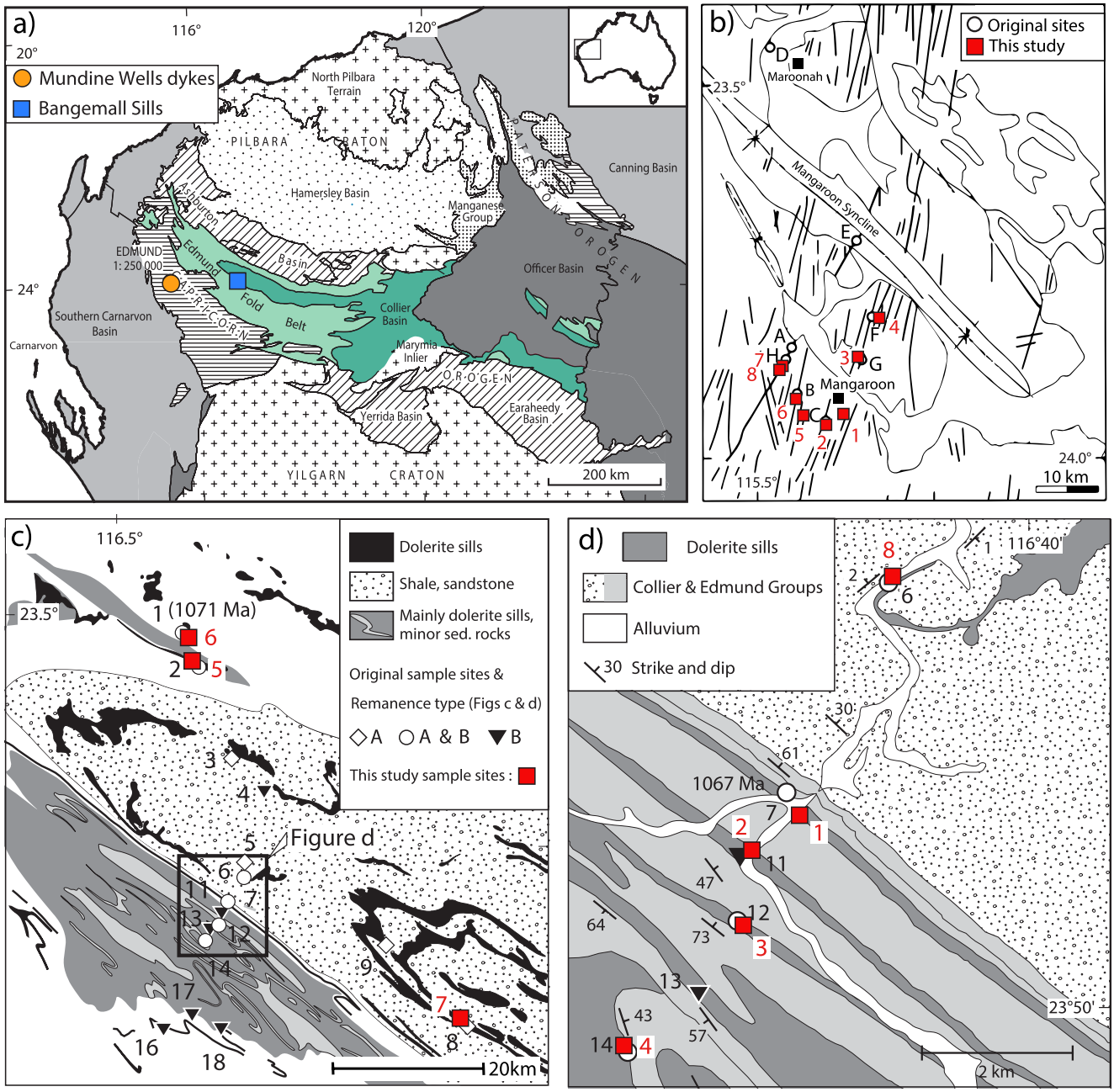

Figure 1. (a) Map showing the geological setting of Mundine Wells dyke swarm (MDS) and Bangemall Sills (BMS) studied here. (b) MDS original paleomagnetic site locations (black open circles) with sites from this study overlaid (solid red squares). (c and d) BMS site locations and remanence types. All maps based on Wingate and Giddings (2000) and Wingate et al. (2002). Original images courtesy of the Geological Survey and Resource Strategy, Department of Mines, Industry Regulation and Safety. © State of Western Australia 2021.

and GPS coordinates although we failed to locate the former drill holes (Figure 1b). An average of eight cores were drilled at each dyke, providing a total of 320 half-inch specimens which were oriented in-situ using a sun compass. The overall mean direction of the MDS dykes here is reported as $D = 014°$, $I = 36°$ ($\alpha 95 = 5°$), with an associated paleopole at 134°E, 44°N (Wingate & Giddings, 2000).

2.2. Background—BMS

The extensive quartz dolerite sills, typically ~100 m thick, are medium-grained with exposed chilled margins. Most samples contain plagioclase, augite, orthopyroxene, and magnetite, with minor quartz and K-feldspar. Some secondary minerals, such as hornblende and biotite, are reported to be the result of deuteric alteration; they are classified geochemically as high-Ti continental tholeiites (Muhling & Brakel, 1985). A paleomagnetic and U–Pb geochronological study of sills was carried out by Wingate et al. (2002) in which statistically indistinguishable ages were obtained (1,071 ± 8, 1,067 ± 14, and 1,068 ± 22 Ma) from three of the sampling sites.

Two types of magnetization were originally identified; type-A, a consistently directed, thermally stable magnetization isolated in 15 sites (including the three dated sills) with magnetite reported as the dominant remanence carrier (Wingate et al., 2002). Type-B magnetization is a chemical remanent magnetization (CRM) most likely carried by maghemite, and is present in several sites alongside type-A.

Site mean directions obtained from type-A magnetization converge after correction for bedding tilt, with an overall mean direction of $D = 339°$, $I = 46.5°$ ($\alpha 95 = 8.3$, $N = 11$). The magnetization is argued to be primary due to multiple factors including positive fold and baked contact tests with no evidence of thermal events that could cause remagnetization. Polarity reversals are also reported between, but not within intrusions (Wingate et al., 2002).

We positively identified and sampled five of the originally studied sills, and a further three sites at the same GPS position as originally reported (Figures 1c and 1d) but where we were unable to locate the original drill holes. An average of eight cores were drilled at five sites, and hand samples were collected in-situ at the remaining three sites. Baked contact was identified at two sites, where a further four cores were drilled. All drill cores were oriented using a sun compass and the combined samples were converted in to 330 half-inch specimens.

3. Methods

The methods laid out in this section apply to both the Mundine and Bangemall localities.

3.1. Rock-Magnetic and SEM

We examined the mineralogy of opaque grains from polished thin-sections (two from each locality) using a low-voltage, high-resolution ZEISS Gemini SEM 460 scanning electron microscope (SEM). Backscattered electron images were taken in combination with Electron Dispersion Spectroscopy (EDS) to identify the composition and condition of the magnetic grains.

Representative rock magnetic measurements were performed on an average of three samples per site. Hysteresis loops, backfield coercivity, saturation Isothermal Remanence Magnetization (sIRM) and high-field thermomagnetic curves of the saturation magnetization, M_s (T), were obtained using a Magnetic Measurements Ltd Variable Field Translation Balance. Hysteresis loops were corrected for the paramagnetic contribution to the slope above 0.5 T, with ratios of the hysteresis parameters, remanent saturation magnetization/saturation magnetization (B_{cr}/B_c) and coercivity of remanence/coercivity (M_{rs}/M_s), used to determine bulk domain stability (Paterson et al., 2017). Curie temperatures (T_C) were calculated using the second derivative of the M_s (T) heating curves with a 3-point running average applied. High-temperature susceptibility, κ (T), experiments were carried out up to 600°C and 700°C using a MFK1-FA Kappabridge susceptometer with CS-3 furnace (AGICO).

3.2. Paleointensity Experiments

A total of 293 individual specimens were subject to paleointensity experiments. Details of specimen labeling are located in the supplementary material. The thermal Thellier method is considered the most robust of paleointensity techniques (Dunlop, 2011) but success rates can be low, particularly with Precambrian rocks (Lloyd, Biggin, et al., 2021). To overcome this and enhance the robustness of the results, a common approach in modern paleointensity studies is to use multiple methods in the acquisition of paleointensity

data (e.g., de Groot et al., 2013; Hawkins et al., 2019; Monster et al., 2015; Yamamoto et al., 2007). We adopt this approach here, utilizing three independent techniques: the thermal Thellier-Coe and IZZI methods (Coe, 1967; Tauxe & Staudigel, 2004), the Shaw double heating technique, in part, with low temperature demagnetization (DHT-LTD; Tsunakawa & Shaw, 1994; Yamamoto et al., 2003) and the Microwave method (Biggin, Perrin, & Dekkers, 2007; Biggin, Perrin, & Shaw, 2007; Hill et al., 2002; Walton et al., 1992).

Thellier and Shaw-DHT measurements were performed using an automated RAPID 2G superconducting rock magnetometer (Morris et al., 2009) in a magnetically shielded cage where the residual field was less than 100 nT. Thermal Thellier experiments were carried out on a total of 57 specimens, consisting of a sequence of paired heatings in air, to a set of increasing temperatures. The IZZI + protocol was used (Tauxe & Staudigel, 2004), which alternates the zero-field and infield steps with partial thermal remanent magnetization (pTRM) checks after every two step pairs. The sequence of steps was repeated up to an average of 590°C, with an infield laboratory bias field of 20 μT and bulk susceptibility measurements taken at every pTRM check. Heatings were carried out in a Magnetic Measurements Ltd MMTDSC super-cooled thermal demagnetizer within the same shielded environment, and specimens were held at temperature for a median 40 min.

The reliability of the Shaw LTD-DHT method has been repeatedly demonstrated using historical lava flows in Hawaii and Japan where the geomagnetic field when the lavas formed is known (Mochizuki et al., 2004; Oishi et al., 2005; Yamamoto & Yamaoka, 2018; Yamamoto et al., 2003). Most experiments in this study are undertaken without the addition of LTD; the use of which was recently found to have no systematic effect on paleointensity results between sister specimens from Precambrian dykes (Lloyd, Biggin, et al., 2021). In this study, 157 specimens were alternating field (AF) demagnetized up to 99 or 100 mT using a Rapid 2G system in a zero-field environment. Anhysteretic remanence magnetization (ARM) was imparted using a DC bias field of between 60 and 70 μT. Laboratory TRMs were imparted by heating to 610°C in a vacuum and maintained at that temperature for various durations ranging from 15 to 35 min (TRM_1) and 15–45 min (TRM_2). Samples were subjected to a DC field of 20 μT throughout the heating and cooling cycle. By varying the hold durations, it helps to ensure that paleointensities and the validation of the ARM alteration corrections are robust. Twenty-six specimens from the BMS sites were subjected to low temperature demagnetization (LTD) treatment, which is known to preferentially target remanence carried by multidomain grains (Yamamoto et al., 2003). These specimens were soaked in liquid nitrogen in a plastic Dewar for 10 min and then removed and allowed to warm to room temperature in a zero field for 60 min. This procedure was carried out prior to the demagnetization of each of the thermal and anhysteretic remanent magnetizations imparted during the Shaw DHT-LTD method (Yamamoto et al., 2003).

A further 80 experiments were carried out on a 14.2 GHz microwave paleointensity system with low-temperature SQUID magnetometer (Suttie et al., 2010). Small cylindrical cores (5 mm diameter) are centered in the resonant cavity, where the microwave field couples with the magnetic system within the sample, producing magnons (quasi-particles associated with spin waves) which demagnetize the sample as the energy is increased. The mechanism of microwave/magnon is analogous to heat/phonon but without significantly heating the bulk specimen. The previously mentioned IZZI+ protocol was used in combination with the quasi-perpendicular method (ChRM makes an angle of at least 45° with the lab field); this achieves a compromise between minimizing any nonideal behavior arising from multi-domain effects while also being able to detect its presence (Hawkins et al., 2019; Yu & Tauxe, 2005). The technique has been demonstrated to produce equivalent results to thermal Thellier-style experiments (e.g., Biggin, Perrin, & Dekkers, 2007; Biggin, Perrin, & Shaw, 2007) and has been successfully used in previous studies (Grappone et al., 2019; Hawkins et al., 2019). Various laboratory fields were used in order to test for any nonlinear TRM effects. The Coe version of the Thellier method (Coe, 1967) incorporating pTRM tail checks (Riisager & Riisager, 2001) was also applied to a very small number of specimens. The tails are a consequence of nonreciprocal thermal blocking and unblocking and their detection might indicate that multi-domain remanence biases the paleointensity estimate.

Our selection criteria are a modified combination of PICTRIT03 (Kissel & Laj, 2004) and MC-CRIT.A1 (Paterson et al., 2015), including, for example, both parameters *f* and FRAC (Table 1). Due to the large overprints associated with these ancient rocks (e.g., Figures 4a and 4e), the *f* criterion is considered appropriate to quantify the required minimum fraction of NRM; however, we maintain that a minimum FRAC

Table 1
Selection Criteria

TH & MW	n	α (°)	MAD (°)	FRAC (%)	f (%)	N_{pTRM}	$\lvert k' \rvert$	β	DRAT (%)	CDRAT (%)
	≥4	≤15	≤10	≥35	≥35	≥2	≤0.25	≤0.11	≤12	≤15
SH	Class	α (°)	MAD (a and f) (°)	FRAC (%)	rN	$\lvert k' \rvert$	f_{RESID}	sT 1 (±)	rT	sA_1 1 (±)
	A	≤10	≤10	≥45	≥0.990	≤0.2	≤0.2	0.05	≥0.990	≤0.4
	B	≤10	≤10	≥45	≥0.990	≤0.2	≤0.2	0.10	≥0.990	≤0.3

Note. Thermal Thellier (TH), Microwave (MW), and Shaw-DHT (SH) selection criteria; used and defined, where possible, according to the standard paleointensity definitions (Paterson et al., 2014). n, number points used in best-fit line; α, angular difference between the anchored and unanchored best-fit directions on the orthogonal diagram; MAD, maximum angular deviation of the (anchored and free) best-fit to the directional data used in an orthogonal diagram (Kirschvink, 1980); FRAC, fraction of NRM used for the best-fit on an Arai diagram (Shaar & Tauxe, 2013); f, fraction of NRM used for the best-fit on an Arai diagram by vector difference sum (Coe et al., 1978); N_{pTRM}, number of partial thermal remanent magnetization (pTRM) checks; q, quality of paleointensity; $\lvert k' \rvert$, curvature of the Arai plot as determined by the best-fit circle to the selected best-fit Arai plot segment (Paterson, 2011); β, a measure of the relative scatter around the best-fit line (standard error of the slope/absolute value of the slope [Coe et al., 1978]); DRAT, maximum absolute difference produced by a pTRM check, normalized by the length of the line (Selkin et al., 2000); CDRAT, Cumulative DRAT (Kissel & Laj, 2004). Shaw-DHT selection criteria parameters are as TH and MW except: rN, R^2 correlation of the paleointensity slope$_{(N)}$; f_{RESID}, defined in the text below; sT, slope$_T$ (TRM_1/TRM_2*; Yamamoto et al., 2003); rT, R^2 correlation of the slope$_T$; sA_1, slope (ARM_0/ARM_1).

must also be present. Three specimens with high f values are accepted with FRAC ≥ 25% (Tables S2 and S5). DRAT and CDRAT are relaxed slightly, but remain strict for use in analyzing ancient rocks (e.g., Kodama et al., 2019). Strict linearity is adhered to in all results ($\lvert k' \rvert \leq 0.25$) with the exception of two MDS specimen results ($\lvert k' \rvert < 0.35$) which produced paleointensities concordant with others and met the other criteria easily.

We expand the typical selection criteria used in analyzing Shaw-DHT data (Yamamoto et al., 2003) to include three additional criteria; these place stricter emphasis on linear, origin-trending paleointensity slopes with limited ARM alteration.

1. $f_{RESID} = \frac{|Y_{int}|}{\Delta Y'}$ (Paterson et al., 2016),

This is an analogy of the NRM fraction (f) of Coe et al. (1978) where Y_{int} is the y-intercept of the paleointensity slope$_{(N)}$ and $\Delta Y'$ is the change in the NRM lost over the selected segment. The criterion quantifies the residual difference between the y-intercept and the origin of the plot. A non-origin trending slope is brought about when NRM and TRM_1* are not unblocking equally and their demagnetization spectra can be fundamentally different shapes (something which is often not determined by the R^2 criterion).

2. $\lvert k' \rvert$ (Paterson, 2011; Paterson et al., 2016)

Defined in Table 1 caption and used in addition to the R^2 correlation, which is not as strict a measure of linearity; this is particularly important in Shaw-DHT pseudo-Arai plots because the paleointensity slope is insensitive to alteration (Tanaka & Komuro, 2009). We apply a strict minimum of $\lvert k' \rvert \leq 0.2$ to all Shaw results (e.g., Lloyd, Paterson, et al., 2021).

3. Slope A_1 (ARM_0/ARM_1) is limited to 1 ± 0.4 thereby limiting the amount of ARM alteration correction accepted and any associated uncertainty, including influences from remanence anisotropy and changes in magnetostatic interactions.

4. Rock Magnetic and SEM Results

4.1. SEM

Backscattered SEM (BSE) images obtained from MDS (Figures 2a–2d) and BMS (Figures 2e–2j) show opaque grains of varying sizes, textures, and oxidation stages. MDS BSE images obtained from site MD6 (Figures 2a–2c) show an area of cross-cutting fine, elongate, low-Ti lamellae (Figure 2a; bottom left); these well-developed lenses are mottled indicating oxidation to stage C4 or C5 (Haggerty, 1991). There is evidence

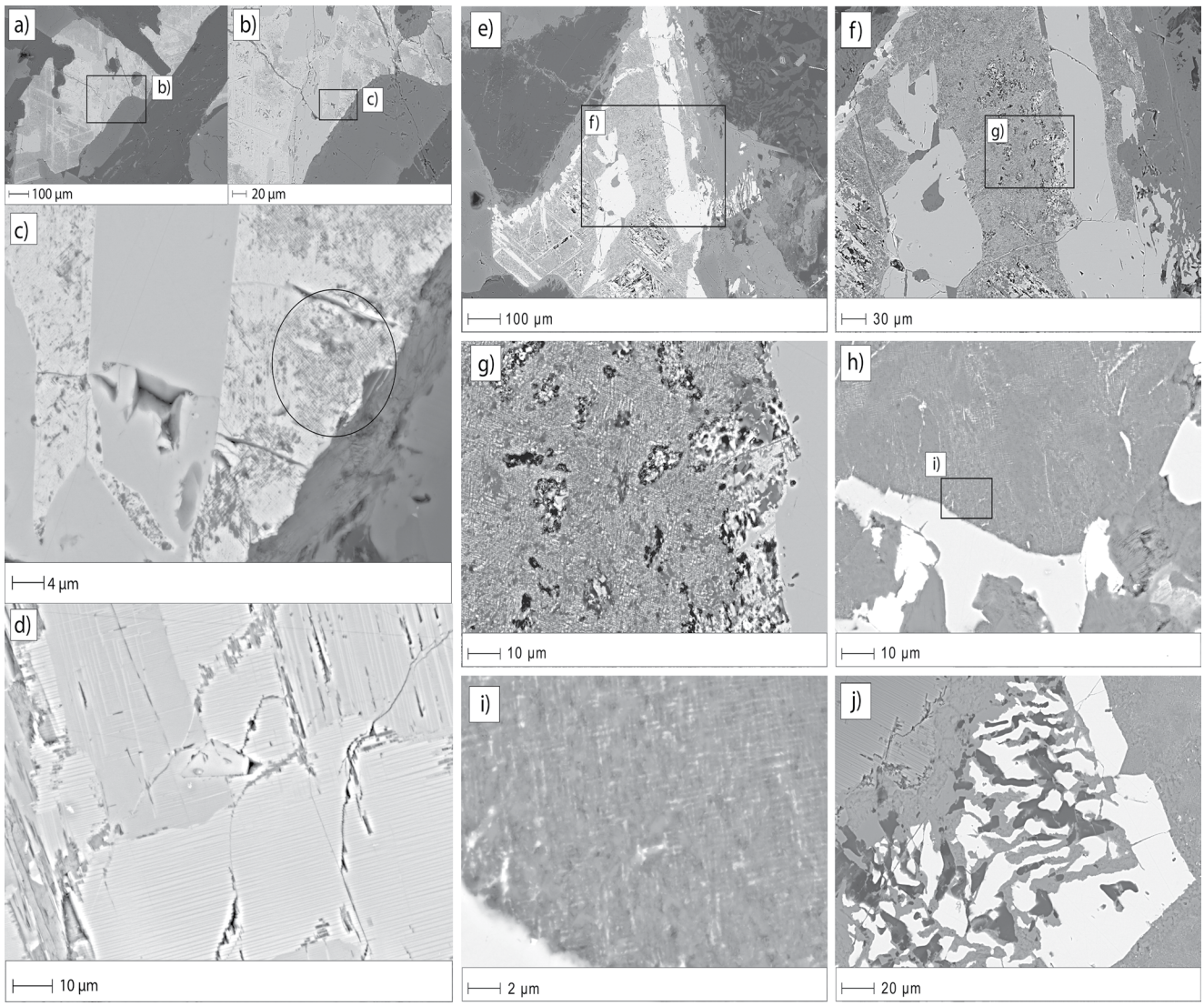

Figure 2. Backscattered scanning electron microscope (SEM) images of typical grain assemblages from Mundine Wells dyke swarm sites MD6 and MD3 (a–c, specimen MD6-4C; d, specimen MD3-4D), and Bangemall Sills site BM7 (e–j, specimen BM7-4B). (a) 100 µm scale image shows a large cluster of opaque grains which contain sub-sets of smaller assemblages. Textures indicate oxidation has occurred to stage C4. (b) 20 µm scale showing cross-cutting elongate lamellae, composed of low and high-Ti phases (left). Textures indicate oxidation has occurred to stage C5. (c) Submicron intergrowths of two phases, interpreted to be low-Ti titanomagnetite and ilmenite, are visible (highlighted). (d) Elongate lamellae are submicron in width are interpreted to consist of low and high-Ti phases. (e–i) Various magnifications show three types of opaque grain; very large (>100 µm) ilmenite, much thinner lathe-like lamellae and very fine intergrowths of two Ti-phases. (j) Large oxy-exsolved ilmenite grain (stage C7) and an area of pristine lamellae which are sub-micron in width (top left).

of cracking, potentially related to low temperature oxidation (Figure 2b); however, $\kappa(T)$ curves do not show notable evidence of maghemite.

At higher resolutions, fine sub-micron trellis intergrowths of two Ti phases are observed (Figure 2c); these are interpreted to be low-Ti titanomagnetite and ilmenite, although EDS analysis could not confirm this. A notably similar pattern is reported in other Precambrian dykes (Hodych, 1996; Smirnov & Tarduno, 2005). These very fine intergrowths suggest oxy-exsolution occurred above or close to the Curie temperature (Haggerty, 1991; Wilson & Watkins, 1967). Perpendicular sets of elongate lamellae, very fine in width, are also observed in site MD3 (Figure 2d) and suggest oxidation to stage C2–3.

BMS BSE images of a specimen from site BM7 show large (~100 µm) ilmenite grains (Figures 2e–2j) to very fine sub-micron intergrowths of two Ti-phases which are present throughout (Figures 2g–2i) and are likely responsible for higher coercivity remanence. There are also lathe-like lamellae present, which vary in

thickness, including some that are submicron in width and appear pristine (Figure 2j; top left). Most grains appear unaltered by low temperature processes and only show evidence only of high-temperature deuteric oxidation which may have progressed to stage C7 in parts (e.g., the decomposition of the large ilmenite grain in Figure 2j).

4.2. Rock Magnetic Results—MDS

The acquired $\kappa\,(T)$ curves are grouped according to quality (Figures 3a and 3b). Site MD5 produces highly nonreversible curves and is omitted from the reported analysis. Large increases and decreases in susceptibility occur in sites MD1, 7, and 8 between ~300 and 350°C which we attribute to the presence of titanomaghemite (Figure 3a). Site MD4 does not produce this feature but is included in the same diagram due its nonreversible results; defined here as > 20% difference between heating and cooling at T_0. Sites MD2, 3, and 6 produce the most reversible curves typical of lower alteration and low-Ti titanomagnetite (Figure 3b). A small susceptibility tail extending beyond 600°C indicates the presence of a small amount of hematite in several specimens, although this is not detected in sIRM results. Most IRM curves saturate in fields less than 300 mT; saturation magnitudes are consistent across sites MD2, 3, and 6, and close to zero in sites MD5, 7, and 8 consistent (Figure 3c).

In the thermomagnetic analysis, Curie temperatures for the main ferrimagnetic phase are found between 560 and 575°C, suggesting that low Ti-titanomagnetite is the magnetic remanence-bearing mineral (Dunlop et al., 1998). The more reversible curves are limited to sites MD2, 3, and 6 with a mean difference between heating and cooling curves of ~20% at T_0 (Figures 3d and 3e); these also produce pronounced Hopkinson peaks indicative of SD grain size distributions (Dunlop, 2014).

Bulk domain stability (BDS) values for sites MD2–6 narrowly exceed the threshold value (0.1) at which reliable paleointensity results are more likely (Paterson et al., 2017). All specimens follow the BDS trend, lying parallel and above it, with specimens from sites 7 and 8 giving uniquely low domain stability values (Figure 3f). Although site MD5 shows a high BDS value, hysteresis curves (Figure S1 in Supporting Information S1) show that these specimens are dominated by a paramagnetic component. The BDS values of the main cluster (sites MD2–4, 6) represent bulk grain distributions in the vortex state range. Nevertheless, pronounced Hopkinson peaks and thermal demagnetization observations (Section 5.1) suggest that some population of SD grains are present.

4.3. Rock Magnetic Results—BMS

Measurements of NRM and bulk susceptibility reveal that specimens from sites BM2–5 are weakly magnetized (~10 mAm^{-1}) with very low bulk susceptibility values (Figure S2 in Supporting Information S1). $\kappa\,(T)$ curves are highly nonreversible in sites BM1–5, with some strong inflections in susceptibility observed at ~300°C; this is particularly apparent in site BM1 (Figures 3g and 3h) and is interpreted to be caused by the presence of titanomaghemite.

Specimens from site BM6 exhibit a mixture of highly nonreversing $\kappa\,(T)$ curves and some with less alteration observed; however, most of the alteration appears to occur at high temperature, between 550°C and 700°C (Figures 3i and 3j). We do not see the same low-temperature inflections associated with titanomaghemite here, although Wingate et al. (2002) report type-A and B magnetization present in this site. Sites BM7 and BM8 produce more reversible $\kappa\,(T)$ curves of varying quality (Figures 3k and 3l); many exhibiting changes in the heating-cooling cycle of less than 10%.

$M_s\,(T)$ curves produce similar results. Sites BM1–5 are highly non-reversible (Figures 3m and 3n). Non-reversible curves are also obtained from sites BM6, 7, and 8 (Figure 3p shows one or two from each site); however, these sites tend to produce more reversible $M_s\,(T)$ curves (most exhibiting a difference of less than 25% at T_0; Figures 3o, 3q and 3r), demonstrating heterogeneity in the samples sets. Curie temperatures for sites BM1–4 range between 590 and 650°C whereas that for BM5 is ~360°C. Site BM6 T_C's range between 570 and 580°C and some, but not all, specimens produce a small step in the curves with an associated T_C of 670°C. Site BM7 T_C's range between 570 and 580°C and site BM8 between 580 and 600°C. The primary T_C's from sites BM6–8 are indicative of magnetite.

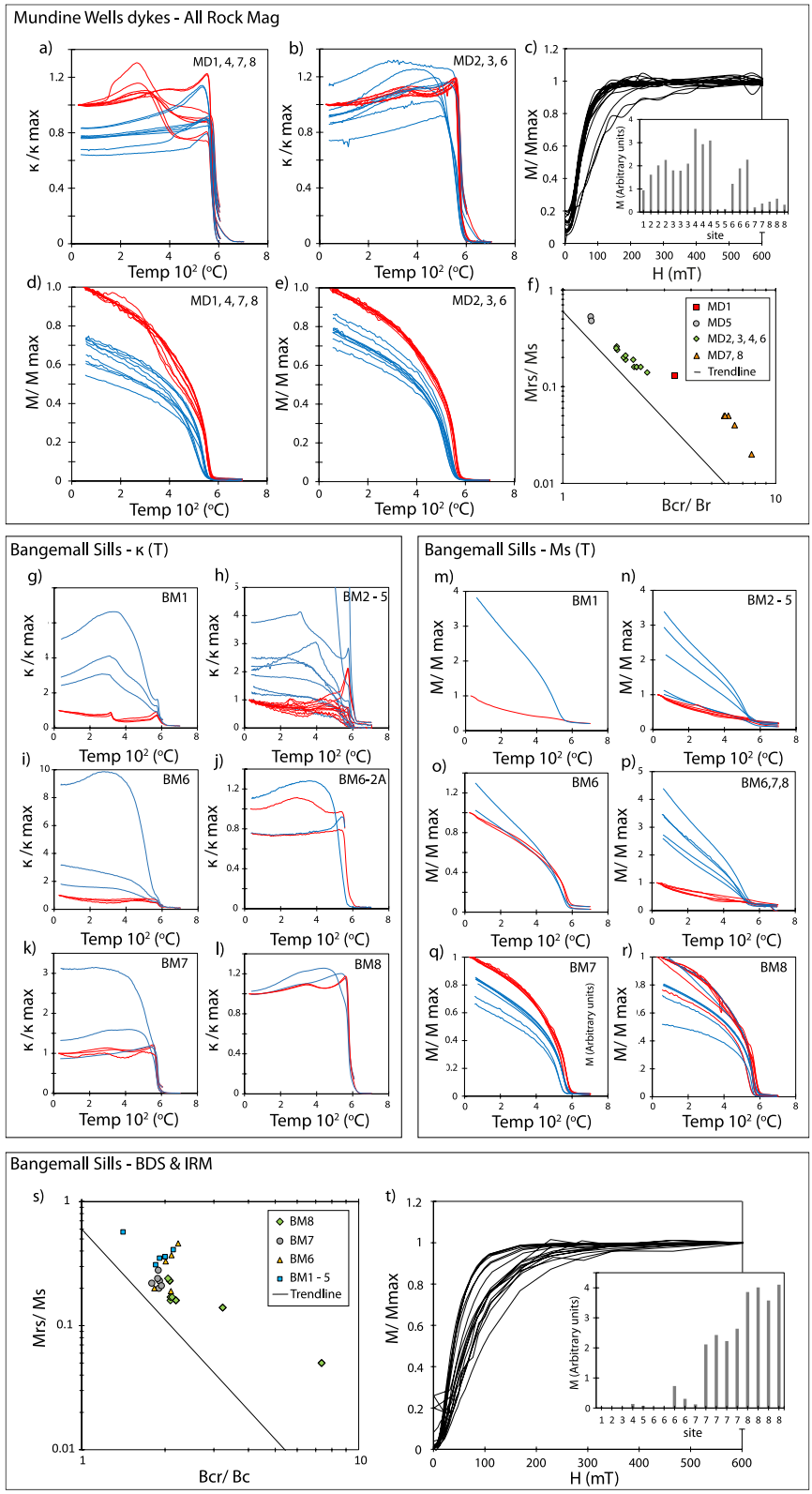

Figure 3.

Table 2
Site Level Results

Site	Ref	Age (Ma)	Type	Lat (°S)	Lon (°E)	Dec (°)	Inc (°)	N (n)	k	a_{95} (°)	F (μT)	σ_F (μT)	n/N_{PI}	N_{mic}	N_{Shaw}	N_{Thel}	VDM Am^2 (10^{22})	σ_{VDM}	Q_{PI}
MD2	EDMC	755	Dyke	23.96	115.61	6.2	38.6	10 (1)	64	6.1	28.9	2.6	2/36	2	-	-	6.29	0.57	7
MD3	EDMG	755	Dyke	23.88	115.64	15.8	33.3	6	205	4.3	28.2	4.7	4/38	3	-	1	6.41	1.08	7
MD6	EDMB	755	Dyke	23.91	115.56	17.2	35.1	11	51	6.6	28.5	4.7	12/33	6	5	1	6.08	1.45	9
BM6	WG1*	1,070	Sill	23.52	116.58	359.8	48.7	9 (3)	75	5.6	3.0	-	1/27	-	1	-	0.60	-	6
BM7	WG8	1,070	Sill	23.94	116.91	343.7	42.9	6	257	3.8	14.3	7.6	12/44	7	5	-	2.98	1.53	8
BM8	WG6	1,070	Sill	23.78	116.56	337.0	35.2	8 (3)	41	8.2	2.9	0.4	3/43	2	1	-	0.64	0.10	8

Note. Summary of paleomagnetic results from both localities. Ref, site reference from original study; *, indicates that our site was close to, but not the exact original site; D (°), magnetic tectonic declination; I (°), magnetic tectonic inclination; N (n), total number of samples given unit weight in calculation of dyke means (number of samples included from baked contact); k, the Fisher precision parameter; a_{95}, 95% confidence limit on the mean direction; F, field intensity; σ_F, absolute standard deviation; N_{PI}, number of paleointensity results; N_{mic}, N_{Shaw}, N_{Thel}, number of results for each respective method; VDM, virtual dipole moment; σ_{VDM}, absolute standard deviation; Q_{PI}, quality score of paleointensity (see Table S7). Directional information taken from Wingate and Giddings (2000) and Wingate et al. (2002).

Mean BDS values for sites BM6 and 7 are 0.15 and 0.12 respectively, while site BM8 mean is 0.07 with some specimens above 0.1 (Figure 3s). IRM curves all saturate in fields less than 300 mT (Figure 3t); saturation magnitudes are close to zero in sites BM1–5 and much higher in sites BM7 and 8, with site BM6 showing variability consistent with other rock magnetic results (Figures 3i, 3j, 3o, 3p and S2 in Supporting Information S1). Hysteresis loops reveal that many specimens from site BM6 are dominated by a paramagnetic signal, which once removed, reveals properties indicative of a small distribution of SD grains (Figure S1 in Supporting Information S1).

5. Paleointensity Results

Extracting paleointensity data from Precambrian rocks is extremely challenging. To ensure that the results are robust and reliable, we apply a relatively strict set of selection criteria to all data (Table 1). Largely as a result of laboratory induced alteration, the overall success rate for both rock units were low: just 34 successful results out of 293 specimens.

5.1. Paleointenstity Results—MDS

A summary of paleointensity results is found in Table 2, and specimen level results in Tables S1–S3. Site-mean paleointensity estimates were determined from the unweighted average of successful results from all methods from a given site.

All specimens from sites MD1, 5, 7, and 8 were rejected after failure of a small number of pilot Shaw-DHT experiments confirmed the poor-quality rock magnetic results. Specimens from these sites suffer from alteration and multi-domain effects (Figures 3a, 3d, and 3f; Table S2). Site MD4 produces slightly scattered paleomagnetic directions (Figure S3 in Supporting Information S1) and no successful paleointensity results.

Figure 3. (a–f) Mundine Wells dyke swarm. (g–t) Bangemall Sills. (a and b) Normalized κ (T) diagrams with specimens from several sites grouped together. Red lines, heating curves; blue lines, cooling curves. (c) Normalized isothermal remanent magnetization (IRM) curves, with inset plot showing the values of saturation magnetization (M_s) for each specimen. (d and e) Normalized M_s (T) diagrams with specimens from several sites grouped together. Red lines, heating curves; blue lines, cooling curves. (f) Bulk domain stability (BDS) diagram with logarithmic scale. M_{rs}/M_s, remanent saturation magnetization/saturation magnetization; Bcr/Bc, coercivity of remanence/coercivity. BDS = (M_{rs}/M_s)/(Bcr/Bc). (g–l) Normalized κ (T) diagrams. (j) Single κ (T) diagram for a specimen from site BM6 which was heated to 550°C, cooled and heated to 700°C. (m–r) Normalized M_s (T) diagrams. (p) Diagram groups non-reversible curves together, from sites BM6, 7 and 8. (s) BDS diagram with logarithmic scale (see Figure 3f). (t) Normalized IRM curves with insert showing magnitude of saturation of individual specimens within the site shown on the x-axis.

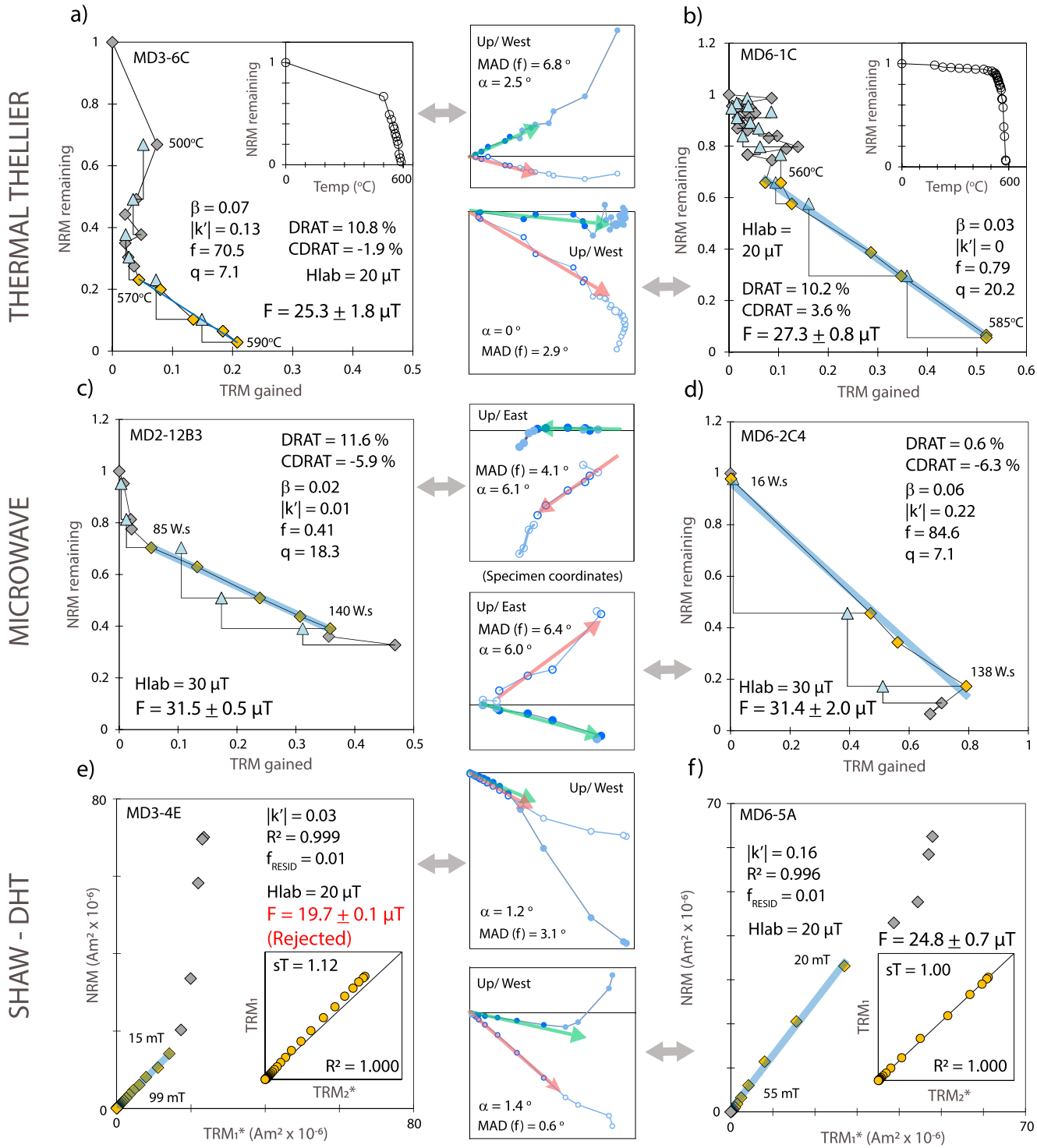

Figure 4. Example Arai/Shaw plots with associated orthogonal plots in geographic coordinates unless otherwise stated (two from each method). (a and b) Thermal Thellier specimens MD3-6C and MD6-1C. (c and d) Microwave specimens MD2-12B3 and MD6-2C4. (e and f) Shaw-DHT specimens MD3-4E and MD6-5A respectively. Thermal Thellier plots include the thermal demagnetization insert. Orange markers, steps used; gray markers, steps not used; light blue triangles, partial thermal remanent magnetization (pTRM) checks; thick blue lines, best-fit line used in paleointensity estimate; red and green lines, best-fit lines determined from principal component analysis of the directional data; *q*, quality factor (Coe et al., 1978). All selection criteria used here are listed in Section 5, Tables 1 and 2.

The only successful results are from sites MD2, 3, and 6 (sites EMBC, G, and B respectively; Wingate & Giddings, 2000); these were difficult to obtain, and success rates for MD2 and 3 are low. AF and thermally demagnetized paleomagnetic directions obtained from this study are found in Figure S3 in Supporting Information S1. Sites MD2 and MD3 are scattered but their means, using a 45° cut-off, are within an angular distance of 20° from those obtained in the original study (Wingate & Giddings, 2000). The MD6 site mean is within 5° of the original and is associated with more precise paleomagnetic directions ($D = 12.6°$, $I = 32.6°$, $k = 64.4$); 12 successful paleointensities are produced from this site (Tables 2 and S1–S3; Figures 4 and S3 in Supporting Information S1).

Results obtained from these three sites are consistently high and in good agreement between and within sites; site mean paleointensity results are within 1 μT of each other (Table 2). All three methods also produced consistent results: Microwave results were obtained from three sites (30.7 ± 4.3 μT; $N = 11$), thermal Thellier results from sites MD3 and MD6 (26.3 ± 1.0 μT; $N = 2$), and Shaw-DHT results from site MD6 only (24.3 ± 1.6 μT; $N = 5$). The highest success rate (35%) was achieved by the Microwave method, compared to 7% from both the thermal Thellier and Shaw-DHT methods.

Successful paleointensities from the thermal Thellier method show that ChRM is unblocked between 560 and 580°C, which could support the presence of a narrow distribution of SD Magnetite grains. This is particularly apparent in the high-quality result ($q = 20.2$) from site MD6 (Figure 4b; Table S1). Although a limited number of results are obtained for sites MD2 and MD3, they pass strict selection criteria and are considered robust; they are also equivalent to the high-quality results from site MD6 (Table 2, Figure 4).

Arai diagrams from site MD3 display two-slope behavior; these account for four specimen results (Figures 4 and S4 in Supporting Information S1 show three of these). The thermal Thellier result (MD3-6C; Figure 4a) suffers severe NRM loss up until ~560°C without acquiring a TRM; after which a notably linear and stable paleointensity slope is obtained. This may be related to its large overprint; similar overprints are observed in many Shaw-DHT specimens, and are generally removed using AF demagnetization by 15 mT (Figures 4e and 4f). It may be possible that they are related to the recently identified "fragile" curvature (Tauxe et al., 2021), however, we think this is unlikely since the paleointensity results are remarkably consistent with all other results, including highly linear, single-slope Arai slopes and across multiple methods (Figures 4b and 4d). For the same reason, we think it unlikely that the grains that unblock at low temperatures are biasing paleointensity results; although they will still contribute to the laboratory-induced remanence. Once the remanence carried by higher coercivity magnetite grains are unblocked, linear paleointensity slopes with values of ~30 μT are observed. These high-power sections of the respective Arai diagrams are associated with origin trending directional data and are interpreted as the ChRM.

A Thellier-Coe experiment with both pTRM and pTRM tail checks was used to determine the extent to which pTRM tails may be influencing the estimates from site MD3. We use the $DRAT_{TAIL}$ criterion (Biggin, Perrin, & Dekkers, 2007; Biggin, Perrin, & Shaw, 2007) to quantify the extent of pTRM tails; the result ($DRAT_{TAIL} = 6.1$; Figure S4b in Supporting Information S1) suggests that pTRM tails are not a significant cause of the two-slope behavior.

The data were tested against a relaxed set of selection criteria (Table S8) to determine whether those applied are reasonable; this allowed 16 additional successful results from Shaw-DHT (11), thermal Thellier (4), and Microwave methods (1). These additional results (Figure S5 in Supporting Information S1) are distinct from those obtained using the stricter criteria. Their inclusion into the overall accepted set of results reduces the site-means for MD2 and MD3 by 20% and 12% respectively, while MD6 would increase by 9%. We maintain that the strict selection criteria are justified and that the results falling outside these criteria should be rejected on the basis that they bias the results slightly. It is worth noting, however, that the number of results would increase by ~50% and that all site-mean paleointensities remain similarly high.

5.2. Paleointensity Results—BMS

A summary of paleointensity results is given in Table 2 and specimen level results in Tables S4–S6. Specimens from five sampling sites (BM1–5) were weakly magnetized (less than 10 mA m^{-1} on average; Figure S2 in Supporting Information S1). In addition, highly non-reversible κ (T) curves (Figures 3g and 3h)

combined with uninterpretable AF demagnetizations of the NRM of selected specimens from these sites, led to a blanket rejection.

Thermal Thellier experiments performed poorly and no results were successful for any specimens from the remaining three sites. Many specimens from site BM6 were too weakly magnetized (10–100 mA m^{-1}) for use on the Microwave system and only a single Shaw-DHT paleointensity (3.0 μT) was obtained that satisfied the selection criteria. This result is equivalent to the weak-intensity results obtained from site BM8 from both Shaw-DHT and Microwave methods (2.9 ± 0.4 μT); however, only three paleointensity results were obtained for this site.

Causes of failure were typically related to alteration rather than MD effects with many Microwave and Shaw-DHT specimen results falling only slightly short of the selection criteria. Microwave experiments produced high DRAT or CDRAT values although these were associated with linear Arai plots; Shaw-DHT specimen results failed in the $slope_N$ correlation rather than $slope_T$ (Tables S5 and S6).

A wide range of results were obtained for site BM7 producing a mean paleointensity of 14.3 ± 7.6 μT ($N = 12$) (Figure 5; Tables 2, S5 and S6). Successful Shaw-DHT specimens from site BM7 require an ARM correction that is small in absolute terms (mean 1.4 μT) as seen in the $slope_{A1}$ values (Table S6). Specimens that underwent LTD treatment produced no successful results and, if we compare narrowly rejected results, we see that LTD treatment was not affecting the paleointensity estimates (Table S6).

Specimens from site BM7 produced linear paleointensity slopes which start at low power (~50 W.s) and slightly low coercivities (10–15 mT; Figure S6 in Supporting Information S1). They are typically fully demagnetized by 120 W.s and 40 mT respectively (Figures 5a–5d). This contrasts with specimens from sites BM6 and BM8 whose characteristic components are isolated above ~100 W.s and which are not fully demagnetized by 200–300 W.s (Figures 5e and 5f). Separating results for site BM7 by method produces a notable difference; Shaw-DHT paleointensities are lower and more precise (7.8 ± 0.9 μT, $N = 5$) compared to the higher and more dispersed Microwave results (18.8 ± 6.4 μT, $N = 7$).

A single, narrowly rejected thermal Thellier result from site BM7 would be in approximate agreement with the site mean result (14.3 μT; Table 2). An estimate of 11.4 μT is obtained, but with high values of DRAT and CDRAT of 25% and 23% respectively (Figure S7 in Supporting Information S1). The alteration produces a trend in pTRM checks which, after applying a correction (Valet et al., 1996), would produces a higher estimate of 16.4 μT (Figure S7 in Supporting Information S1); however, we note that this result is not robust.

5.3. Q_{PI} Results

Successful site-mean results are assessed using the Q_{PI} system (Biggin & Paterson, 2014). Previous comprehensive paleomagnetic studies combine with modern paleointensity techniques here to produce high overall site scores of between 6 and 9 for both localities (Tables 2 and S7). Well-defined directions are associated with primary remanent magnetization and accurate U-Pb ages (Wingate & Giddings, 2000; Wingate et al., 2002). SEM images also suggest that the remanences are primary (Figure 2). Paleointensity techniques test for, or remain clear of, alteration and MD effects. This is achieved through pTRM checks, pTRM tail checks and ARM corrections, and is supported by rock magnetic results (Figures 3b, 3e, 3k, 3l, 3q, and 3r). Additionally, there is reasonable evidence that the final estimate was not significantly biased by anisotropy of TRM, cooling rate effects, or nonlinear TRM effects. This is provided by low γ-values, evidence of PSV grain size distributions (Figures 3f and 3s) that are unlikely to be strongly affected by cooling rate differences (Biggin et al., 2013), and varying the applied field strength in alternate experiments respectively.

6. Discussion

Paleointensity results are obtained from three cooling units for each studied rock target. MDS results are remarkably consistent, however the results for BMS are lower quality and a difference can be observed according to the method used (Figure S8 in Supporting Information S1). Multiple lines of evidence support the presence of primary thermal remanence magnetization in both targets (Wingate & Giddings, 2000; Wingate et al., 2002), including the new SEM evidence. Both MDS and BMS produced well-defined mean paleopoles which have been used for plate reconstructions. It is uncertain, however, whether the associated

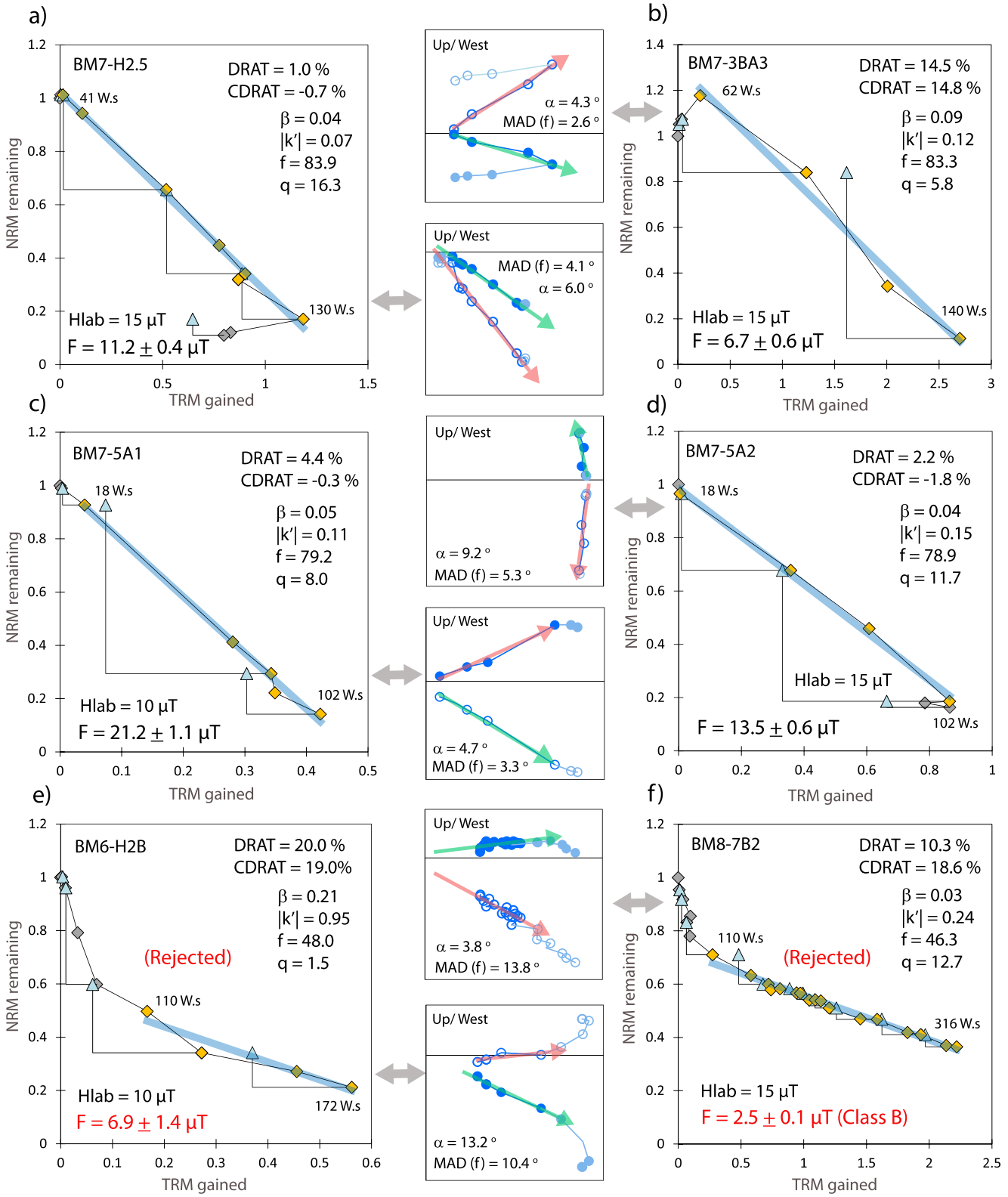

Figure 5. Microwave example Arai diagrams and associated orthogonal diagrams in specimen coordinates. (a–d) Example results from site BM7 showing the variation seen in the Microwave results from this site. (e and f) Rejected specimen results from sites BM6 and BM8 respectively. Specimens from these sites demagnetize at noticeably higher power than those in site BM7. Plot descriptions are the same as for Figure 4.

paleointensity results are sufficiently time-averaged and capture the true dipole strength rather than extremes of paleosecular variation. It should be noted that BMS directions of opposite polarity (original sample site 25; Wingate et al., 2002) imply that the intrusive event spanned at least one reversal of the Earth's magnetic field, suggesting that the type-A magnetizations are adequately averaging paleosecular variation.

6.1. MDS

MDS rock magnetic and paleointensity results are consistent; sites from which we observe more reversible M_s (T) and κ (T) curves (Figure 3) also produce the successful paleointensities (Figures 3, 4 and S4 in Supporting Information S1; Tables S1–S3). Backscatter SEM images show submicron intergrowths of magnetite (Figure 2c), which are attributed to the thermal demagnetization of a narrow distribution of SD remanence in sites MD3 and MD6. Evidence of occasional alteration cracking in some larger grains from samples in sites MD2 and 3 may be the cause of the lower overall success rates in these sites. The paleointensity results obtained from MD2, 3, and 6 are high and in excellent agreement within and between site (and method). Application of strict selection criteria improves the results, by avoiding what appear to be slightly biased results (Figure S5 in Supporting Information S1). Paleomagnetic directions from these sites are consistent with other MDS sites and those from the Northampton block (Embleton & Schmidt, 1985; Wingate & Giddings, 2000). The consistent directions combined with positive baked contact tests rule out IRM as the source of the high paleointensities (Wingate & Giddings, 2000).

Two-slope (rather than sagging) Arai diagrams seen in some specimens from site MD3 (Figures 4a and S4 in Supporting Information S1) are a common phenomenon in Thellier paleointensity results which is not well-understood (Kosterov & Prévot, 1998; Sprain et al., 2018; Tauxe et al., 2021). The slope values associated with the low-power/temperature section of the Arai plot can be attributed to overprint if the values are Earth-like. These sections do correspond to overprint regions in the orthogonal diagrams (e.g., Figure 4a), however, the intensity values associated would be too high. This would be true of any high intensities with two-slope behavior, and although this may be related to MD remanence or some form of annealing (Kosterov & Prévot, 1998), it is more likely to be a moderate IRM overprint.

VDMs from all three sites range between 5.3 and 6.7 $Am^2 \times 10^{22}$ with standard deviations of less than 1.5 $Am^2 \times 10^{22}$ (Table 2), similar in strength to the uniquely high MCR results from ~325 Myr earlier. Results which provide evidence of a strong geomagnetic field in the mid-Neoproterozoic are not expected if ICN has yet to occur, as suggested by recent models (Bono et al., 2019; Driscoll, 2016). At this time, the available thermal energy is estimated to have decreased to a level which could only sustain a weakly powered geodynamo.

6.2. BMS

Despite carrying out experiments on 165 individual specimens, the number of results from the BMS is less than ideal, particularly since we must rely on just three out of eight sites for paleointensity. Intensity estimates from site BM8 are very weak and site BM6 produces just a single result (also weak). In contrast, site BM7 produces many more results with a notably higher mean and large within-site dispersion.

Site BM7 was originally interpreted to be of higher quality with only type-A magnetization reported (Wingate et al., 2002). Rock magnetic results suggest that there is localized heterogeneity within-site (Figures 3k, 3p, and 3q). Furthermore, SEM results show that specimens contain a mixture of grain assemblages (Figure 2) which may be responsible for the high within-site scatter seen in paleointensity results. In agreement, high and low microwave paleointensities are obtained from the same mother samples (core 5, samples A and C and core H2; Table S5). No specific correlation can therefore be made, between rock magnetic results and particular paleointensity values.

With such few results from sites BM6 and BM8, and high dispersion in site BM7, we examine results with certain selection criteria relaxed to determine if any qualitative value can be obtained. We note that site BM6 includes a further five Shaw-DHT results which were rejected due to failure of the $slope_T$ criterion alone. These specimens produced well-correlated ($R^2 \geq 0.990$) and linear ($|k'| \leq 0.2$) paleointensity slopes. They are also associated with accurate paleomagnetic directions (Table S6) obtained from type-A (primary,

thermally stable magnetization; Wingate et al., 2002) and SD-type hysteresis loops (Figure S1 in Supporting Information S1). We can quantify the errors associated with specimens that only fail the slope$_T$ criterion.

A nonunit slope$_T$ places a potential lower or upper bound on the paleointensity estimate; for example, a slope$_T$ of 0.70 suggests that the associated paleointensity may under-estimate the field by up to 30%. For weak paleointensity estimates, the equivalent absolute error value is small; the five rejected results would produce a mean paleointensity of 6.6 ± 1.6 μT, however, their low slope$_T$ values suggest an upper bound of 8.9 μT ± 1.8 μT (Table S6). These narrowly rejected, consistent results suggest that site BM6 was recording a weak paleofield at this time. While we do not determine this site robust enough to report a VDM, these results are remarkably similar to Shaw-DHT results from site BM7 (7.8 ± 0.9 μT, $N = 5$), and relatively close, in absolute terms, to the results from site BM8 (2.9 ± 0.4 μT, $N = 3$). It may be possible that the large scatter associated with site BM7 microwave data is due to the much smaller specimens containing heterogeneous abundances of particular magnetic minerals.

Site BM8 produces consistently more reversible $\kappa(T)$ curves, with specimens demagnetizing at high power and coercivities; these are likely to be associated with the fine, pristine opaque grains observed in the backscatter SEM images. The paleointensity results, obtained from two methods, are precise and very weak. The evidence, therefore, suggests that the results from this site are robust.

We arrive at the conclusion that reasonable site mean paleointensities are obtained for sites BM7 and BM8, which produce VDM's of 3.0 and 0.6 $Am^2 \times 10^{22}$ respectively (Table 2). Site BM6 produces a single specimen result and is therefore rejected. We tentatively suggest that a conservative estimate for this site is would be 1.8 ± 0.4 $Am^2 \times 10^{22}$ (based on a 9 μT upper bound mean) and note that this would support a mean VDM from the accepted sites (1.8 ± 1.2 $Am^2 \times 10^{22}$). This reenforces our interpretation that these sills are recording a moderately weak field at this time. At 1,070 ± 6 Ma, the BDS results are concordant with a long-term decreasing trend associated with a decaying thermal regime in a fully liquid core (Figure 6a; Bono et al., 2019). They are, however, at odds with the considerably higher dipole moment values obtained at a similar time (~1,087 Ma) from the Mid-Continent Rift.

6.3. Implications for the Precambrian Geodynamo

Little is known about Precambrian dipole moment variability on any time scale. While we cannot rule out the possibility that our results are biased by short-term deviations from the time-averaged field, these new combined results suggest that the variability of the field on timescales tens of millions of years may have been similar in the Precambrian to that observed in the Phanerozoic.

We compare VDM results (Figure 6a) from MDS at ~755 Ma (6.3 ± 0.1 $Am^2 \times 10^{22}$) with those from the Franklin LIP at ~720 Ma (1.0 ± 0.5 $Am^2 \times 10^{22}$; Lloyd, Biggin, et al., 2021). These two data sets are from the spatially distinct paleocontinents of Australia and Laurentia. We also compare the weak VDM results from BMS at 1,070 ± 6 Ma (1.8 ± 1.2 $Am^2 \times 10^{22}$) which are at odds with those from the MCR at 1,087 ± 2 Ma (5.4 ± 1.2 $Am^2 \times 10^{22}$; $N \geq 3$; Kulakov et al., 2013; Sprain et al., 2018). The data in these two comparisons are separated temporally by ~35 and ~17 Ma respectively, and would require significant changes in field intensity or dipole behavior to explain the extreme contrast.

These Precambrian variations are similar to, or greater than, those seen for much younger time periods populated by larger data sets; for example, two ~5 Ma (0.05–5 Ma and 10–15 Ma) average VDM values (6.9 ± 2.8 $Am^2 \times 10^{22}$ and 3.6 ± 1.7 $Am^2 \times 10^{22}$) were compared by Smirnov (2017).

A Precambrian study of PSV (which include BMS; Smirnov et al., 2011) of the time period 1.0–2.2 Ga produces the Model G (McFadden et al., 1988) parameters $a = 11.1 \pm 1.5°$ and $b = 0.21 \pm 0.09$, where a and b are constants that quantify the scatter of virtual geomagnetic poles at the equator and its rate of increase with paleolatitude respectively. When we compare these with recently calculated parameters for the last 10 Ma ($a = 11.3 \pm 1.3°$ and $b = 0.27 \pm 0.08$; Cromwell et al., 2018; Doubrovine et al., 2019) we see that the "a" parameter values are indistinguishable. This supports that, on average, the axial dipole was similarly dominant over higher-order fields (Biggin et al., 2020) in the Precambrian as it was in the last 10 Ma.

Analysis of current PINT data indicate that the field was slightly less variable in the Precambrian compared with younger periods (Figure 6b); however, the data are so sparsely populated that it is likely that variability

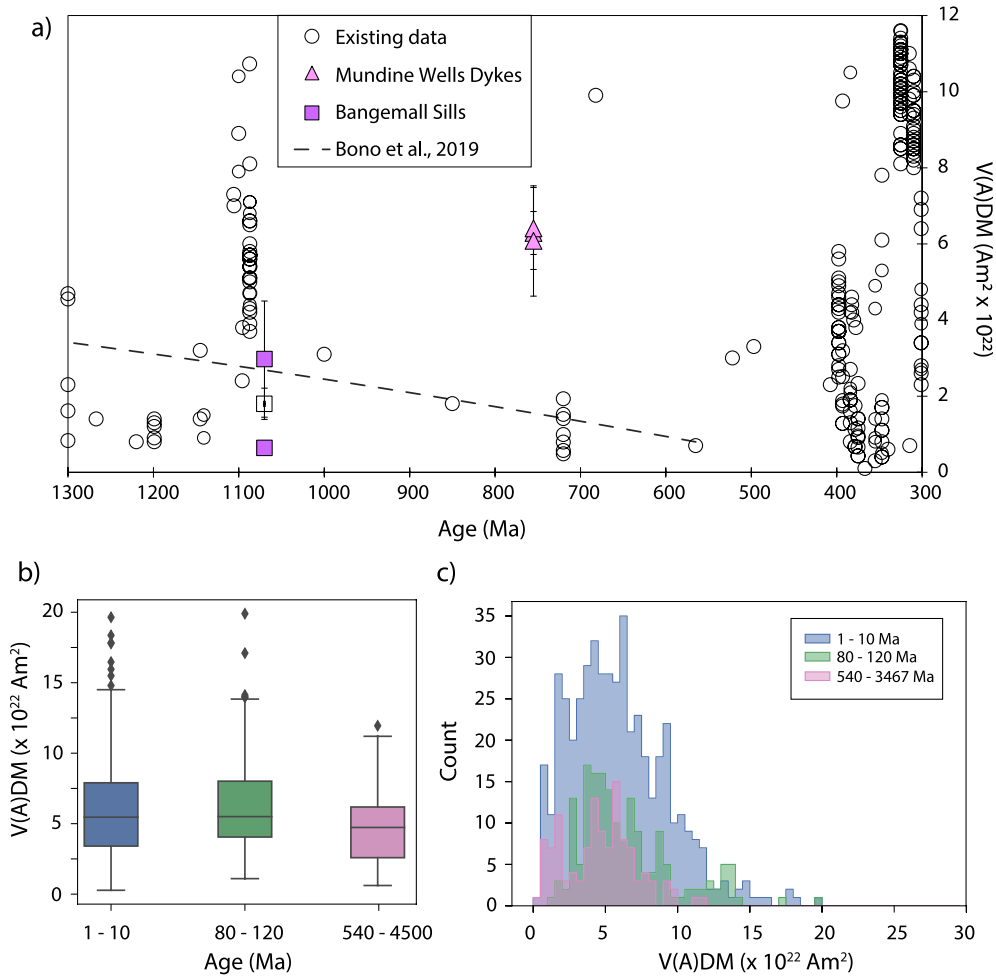

Figure 6. (a) Global database of virtual (axial) dipole moments taken from the PINT database (v.2015.05; http://earth.liv.ac.uk/pint/; Biggin et al., 2015) for the period 300–1,300 Ma. All existing data prior to 500 Ma is filtered so that each cooling unit has $N \geq 3$. All data ≥500 Ma is also filtered by $Q_{PI} \geq 3$ (Biggin et al., 2015). Second order polynomial best-fit line from Bono et al. (2019), dashed line. BDS site BM6 is depicted (square outline) for context only. (b) Box and whisker plot of virtual (axial) dipole moments taken from the PINT database (v.2015.05; http://earth.liv.ac.uk/pint/; Biggin et al., 2015) separated into three time periods ($N \geq 3$). (c) Distribution of virtual (axial) dipole moments over similar time periods (labeled).

is not fully captured. The distribution of dipole moments is also remarkably similar but the amount of data for the last 10 Ma is almost five times greater than for the entire Precambrian (Figure 6c).

We therefore identify multiple similarities between the Precambrian field and that of the last 10 Ma: distribution of dipole moments, average variability in PINT, dipole dominance inferred from PSV data, and from this study, large changes in dipole moment apparent on timescales of tens of Myr. Observational parameters such as paleointensity act as a constraint on numerical dynamo simulations which aim to solve many deep earth problems in the ancient past, including events such as ICN (Biggin et al., 2015; Bono et al., 2019). However, it appears that the data coverage in the Precambrian may be insufficient to accurately average the field in order to use with an acceptable level of uncertainty.

7. Conclusions

We have obtained new paleointensity measurements from two important periods in the Precambrian era. Weak site-mean intensities (3 and 14 μT) are obtained from two Bangemall Sills at 1,070 ± 6 Ma with VDMs of 0.6 and 3 $Am^2 \times 10^{22}$. An additional sill provides a single weak intensity (3 μT) with evidence to suggest

the true value may be closer to 9 μT; an amended VDM from this sill would be equivalent to the mean of the two accepted VDMs. These new weak-field results are in stark contrast with the strong field reported at 1,087 Ma, suggesting that the field was highly variable at this time. The higher of these new results are also concordant with a long-term decaying dipole trend.

At 755 ± 3 Ma, three MDS sites produce a high-fidelity paleointensity results of 28.5 ± 0.3 μT and equally precise VDMs of 6.3 ± 0.1 $Am^2 \times 10^{22}$. Results are consistent within and between-site, and from three independent techniques; they are also associated with high Q_{PI} scores between 7 and 9. A strong field at this time, at face value, does not support recent predictions of a young inner core and is highly distinct to recently reported mid-Neoproterozoic weak intensities from the Franklin Large Igneous Province (Lloyd, Biggin, et al., 2021).

These combined new data allow for comparisons with existing data that are from rocks differing in age by 17 and 35 Myr. They suggest that Precambrian field variability is similar to that observed in more recent times. With severe paucity in global records, particularly for the Neoproterozoic era, it is therefore likely that paleointensities may capture only part of a highly variable field. Using spatial or temporal anomalies as a proxy for events such as ICN may not be robust until many further data is obtained.

Data Availability Statement

S. Lloyd, A. Biggin, Z.-X. Li (2021), "New paleointensity data suggest possible Phanerozoic-type geomagnetic variations in the Precambrian," Magic Information Consortium (MagIC), doi: 10.7288/V4/MAGIC/17452.

Acknowledgments
Simon J. Lloyd and Andrew J. Biggin acknowledge funding from The Leverhulme Trust (RLA-2016-080) and Simon J. Lloyd, Andrew J. Biggin, and Zheng-Xiang Li further acknowledge NERC directed funding (NE/S008330/1). Zheng-Xiang Li also acknowledge support from the Australian Research Council (grants FL150100133 to Zheng-Xiang Li, and DP210102495 to Zheng-Xiang Li and Andrew J. Biggin).

References

Biggin, A. J., Badejo, S., Hodgson, E., Muxworthy, A. R., Shaw, J., & Dekkers, M. J. (2013). The effect of cooling rate on the intensity of thermoremanent magnetization (TRM) acquired by assemblages of pseudo-single domain, multidomain and interacting single-domain grains. *Geophysical Journal International*, *193*(3), 1239–1249. https://doi.org/10.1093/gji/ggt078

Biggin, A. J., & Böhnel, H. N. (2003). A method to reduce the curvature of Arai plots produced during Thellier palaeointensity experiments performed on multidomain grains. *Geophysical Journal International*, *155*(3), F13–F19. https://doi.org/10.1111/j.1365-246X.2003.02089.x

Biggin, A. J., Bono, R., Meduri, D., Sprain, C., Davies, C., Holme, R., & Doubrovine, P. (2020). Quantitative estimates of average geomagnetic axial dipole dominance in deep geological time. *Nature Communications*. https://doi.org/10.1038/s41467-020-19794-7

Biggin, A. J., de Wit, M. J., Langereis, C. G., Zegers, T. E., Voûte, S., Dekkers, M. J., & Drost, K. (2011). Palaeomagnetism of Archaean rocks of the Onverwacht Group, Barberton Greenstone Belt (southern Africa): Evidence for a stable and potentially reversing geomagnetic field at ca. 3.5 Ga. *Earth and Planetary Science Letters*, *302*(3–4), 314–328. https://doi.org/10.1016/j.epsl.2010.12.024

Biggin, A. J., & Paterson, G. A. (2014). A new set of qualitative reliability criteria to aid inferences on palaeomagnetic dipole moment variations through geological time. *Frontiers in Earth Science*, *2*, 1–9. https://doi.org/10.3389/feart.2014.00024

Biggin, A. J., Perrin, M., & Dekkers, M. J. (2007). A reliable absolute palaeointensity determination obtained from a non-ideal recorder. *Earth and Planetary Science Letters*, *257*(3–4), 545–563. https://doi.org/10.1016/j.epsl.2007.03.017

Biggin, A. J., Perrin, M., & Shaw, J. (2007). A comparison of a quasi-perpendicular method of absolute palaeointensity determination with other thermal and microwave techniques. *Earth and Planetary Science Letters*, *257*(3–4), 564–581. https://doi.org/10.1016/j.epsl.2007.03.016

Biggin, A. J., Piispa, E. J., Pesonen, L. J., Holme, R., Paterson, G. A., Veikkolainen, T., & Tauxe, L. (2015). Palaeomagnetic field intensity variations suggest Mesoproterozoic inner-core nucleation. *Nature*, *526*(7572), 245–248. https://doi.org/10.1038/nature15523

Bono, R. K., Tarduno, J. A., Nimmo, F., & Cottrell, R. D. (2019). Young inner core inferred from Ediacaran ultra-low geomagnetic field intensity. *Nature Geoscience*, *12*(2), 143–147. https://doi.org/10.1038/s41561-018-0288-0

Coe, R. S. (1967). The determination of paleo-intensities of the Earth's magnetic field with emphasis on mechanisms which could cause non-ideal behavior in Thellier's method. *Journal of Geomagnetism and Geoelectricity*, *19*(3), 157–179. https://doi.org/10.5636/jgg.19.157

Coe, R. S., Grommé, S., & Mankinen, E. A. (1978). Geomagnetic paleointensities from radiocarbon-dated lava flows on Hawaii and the question of the Pacific nondipole low. *Journal of Geophysical Research*, *83*(B4), 1740–1756. https://doi.org/10.1029/jb083ib04p01740

Cromwell, G., Johnson, C. L., Tauxe, L., Constable, C. G., & Jarboe, N. A. (2018). PSV10: A global data set for 0–10 Ma time-averaged field and paleosecular variation studies. *Geochemistry, Geophysics, Geosystems*, *19*(5), 1533–1558. https://doi.org/10.1002/2017GC007318

Doubrovine, P. V., Veikkolainen, T., Pesonen, L. J., Piispa, E., Ots, S., Smirnov, A. V., et al. (2019). Latitude dependence of geomagnetic paleosecular variation and its relation to the frequency of magnetic reversals: Observations from the Cretaceous and Jurassic. *Geochemistry, Geophysics, Geosystems*, *20*(3), 1240–1279. https://doi.org/10.1029/2018GC007863

Driscoll, P. E. (2016). Simulating 2 Ga of geodynamo history. *Geophysical Research Letters*, *43*(11), 5680–5687. https://doi.org/10.1002/2016GL068858

Dunlop, D. J. (2011). Physical basis of the Thellier-Thellier and related paleointensity methods. *Physics of the Earth and Planetary Interiors*, *187*(3–4), 118–138. https://doi.org/10.1016/j.pepi.2011.03.006

Dunlop, D. J. (2014). High-temperature susceptibility of magnetite: A new pseudo-single-domain effect. *Geophysical Journal International*, *199*(2), 707–716. https://doi.org/10.1093/gji/ggu247

Dunlop, D. J., Özdemir, Ö., & Fuller, M. D. (1998). Rock magnetism: Fundamentals and frontiers. *Physics Today*, *51*, 64–66. https://doi.org/10.1063/1.882466

Embleton, B. J. J., & Schmidt, P. W. (1985). Age and significance of magnetizations in dolerite dykes from the northampton block, western australia. *Australian Journal of Earth Sciences*, *32*(3), 279–286. https://doi.org/10.1080/08120098508729330

Grappone, J. M., Biggin, A. J., & Hill, M. J. (2019). Solving the mystery of the 1960 Hawaiian lava flow: Implications for estimating Earth's magnetic field. *Geophysical Journal International*, *218*(3), 1796–1806. https://doi.org/10.1093/gji/ggz252

de Groot, L. V., Mullender, T. A. T., & Dekkers, M. J. (2013). An evaluation of the influence of the experimental cooling rate along with other thermomagnetic effects to explain anomalously low palaeointensities obtained for historic lavas of Mt Etna (Italy). *Geophysical Journal International*, *193*, 1198–1215. https://doi.org/10.1093/gji/ggt065

Haggerty, S. E. (1991). Chapter 5.Oxide textures—A mini-atlas. In *Oxide minerals* (pp. 129–220). https://doi.org/10.1515/9781501508684-008

Hawkins, L. M. A., Anwar, T., Shcherbakova, V. V., Biggin, A. J., Kravchinsky, V. A., Shatsillo, A. V., & Pavlov, V. E. (2019). An exceptionally weak Devonian geomagnetic field recorded by the Viluy Traps, Siberia. *Earth and Planetary Science Letters*, *506*, 134–145. https://doi.org/10.1016/j.epsl.2018.10.035

Hill, M. J., Gratton, M. N., & Shaw, J. (2002). A comparison of thermal and microwave palaeomagnetic techniques using lava containing laboratory induced remanence. *Geophysical Journal International*, *151*(1), 157–163. https://doi.org/10.1046/j.1365-246X.2002.01745.x

Hodych, J. P. (1996). Inferring domain state from magnetic hysteresis in high coercivity dolerites bearing magnetite with ilmenite lamellae. *Earth and Planetary Science Letters*, *142*, 523–533. https://doi.org/10.1016/0012-821x(96)00107-0

Kirschvink, J. L. (1980). The least-squares line and plane and the analysis of palaeomagnetic data. *Geophysical Journal of the Royal Astronomical Society*, *62*, 699–718. https://doi.org/10.1111/j.1365-246X.1980.tb02601.x

Kissel, C., & Laj, C. (2004). Improvements in procedure and paleointensity selection criteria (PICRIT-03) for Thellier and Thellier determinations: Application to Hawaiian basaltic long cores. *Physics of the Earth and Planetary Interiors*, *147*(2–3), 155–169. https://doi.org/10.1016/j.pepi.2004.06.010

Kodama, K. P., Carnes, L. K., Tarduno, J. A., & Berti, C. (2019). Palaeointensity of the 1.3 billion-yr-old Gardar basalts, southern Greenland revisited: No evidence for onset of inner core growth. *Geophysical Journal International*, *217*(3), 1974–1987. https://doi.org/10.1093/gji/ggz126

Kosterov, A. A., & Prévot, M. (1998). Possible mechanisms causing failure of Thellier palaeointensity experiments in some basalts. *Geophysical Journal International*, *134*(2), 554–572. https://doi.org/10.1046/j.1365-246X.1998.00581.x

Kulakov, E. V., Sprain, C. J., Doubrovine, P. V., Smirnov, A. V., Paterson, G. A., Hawkins, L., et al. (2019). Analysis of an updated paleointensity database (QPI-PINT) for 65–200 Ma: Implications for the long-term history of dipole moment through the Mesozoic. *Journal of Geophysical Research: Solid Earth*, *124*(10), 9999–10022. https://doi.org/10.1029/2018JB017287

Kulakov, E. V., Smirnov, A. V., & Diehl, J. F. (2013). Absolute geomagnetic paleointensity as recorded by ~1.09 Ga Lake Shore Traps (Keweenaw Peninsula, Michigan). *Studia Geophysica et Geodaetica*, *57*(4), 565–584. https://doi.org/10.1007/s11200-013-0606-3

Li, Z. X., Bogdanova, S. V., Collins, A. S., Davidson, A., De Waele, B., Ernst, R. E., et al. (2008). Assembly, configuration, and break-up history of Rodinia: A synthesis. *Precambrian Research*, *160*(1–2), 179–210. https://doi.org/10.1016/j.precamres.2007.04.021

Lloyd, S. J., Biggin, A. J., Halls, H., & Hill, M. J. (2021). First palaeointensity data from the cryogenian and their potential implications for inner core nucleation age. *Geophysical Journal International*, *226*, 66–77. https://doi.org/10.1093/gji/ggab090

Lloyd, S. J., Paterson, G. A., Thallner, D., & Biggin, A. J. (2021). Improvements to the Shaw-type absolute palaeointensity method. *Frontiers in Earth Science*, *9*, 1–11. https://doi.org/10.3389/feart.2021.701863

McFadden, P. L., Merrill, R. T., & Mcelhinny, M. W. (1988). Dipole/quadrupole family modeling of paleosecular variation. *Journal of Geophysical Research*, *93*(7), 11583–11588. https://doi.org/10.1029/jb093ib10p11583

Meert, J. G., & Torsvik, T. H. (2003). The making and unmaking of a supercontinent: Rodinia revisited. *Tectonophysics*, *375*(1–4), 261–288. https://doi.org/10.1016/S0040-1951(03)00342-1

Mochizuki, N., Tsunakawa, H., Oishi, Y., Wakai, S., Wakabayashi, K., & Yamamoto, Y. (2004). Palaeointensity study of the Oshima 1986 lava in Japan: Implications for the reliability of the Thellier and LTD-DHT Shaw methods. *Physics of the Earth and Planetary Interiors*, *146*(3–4), 395–416. https://doi.org/10.1016/j.pepi.2004.02.007

Monster, M. W. L., Groot, L. V. D., Biggin, A. J., & Dekkers, M. J. (2015). The performance of various palaeointensity techniques as a function of rock magnetic behaviour—A case study for La Palma. *Physics of the Earth and Planetary Interiors*, *242*, 36–49. https://doi.org/10.1016/j.pepi.2015.03.004

Morris, E. R., Schillinger, W., Coe, R. S., Pluhar, C. J., & Jarboe, N. A. (2009). Automating the 2G superconducting rock magnetometer for single-solenoid alternating field demagnetization. *Geochemistry, Geophysics, Geosystems*, *10*(5). https://doi.org/10.1029/2008GC002289

Muhling, P. C., & Brakel, A. T. (1985). Geology of the Bangemall Group—The evolution of an intracratonic Proterozoic basin. *Geological Survey of Western Australia Bulletin*, *128*, 1–219.

Oishi, Y., Tsunakawa, H., Mochizuki, N., Yamamoto, Y., Wakabayashi, K. I., & Shibuya, H. (2005). Validity of the LTD-DHT Shaw and Thellier palaeointensity methods: A case study of the Kilauea 1970 lava. *Physics of the Earth and Planetary Interiors*, *149*(3–4), 243–257. https://doi.org/10.1016/j.pepi.2004.10.009

Paterson, G. A. (2011). A simple test for the presence of multidomain behavior during paleointensity experiments. *Journal of Geophysical Research*, *116*(10), 1–12. https://doi.org/10.1029/2011JB008369

Paterson, G. A., Biggin, A. J., Hodgson, E., & Hill, M. J. (2015). Thellier-type paleointensity data from multidomain specimens. *Physics of the Earth and Planetary Interiors*, *245*, 117–133. https://doi.org/10.1016/j.pepi.2015.06.003

Paterson, G. A., Heslop, D., & Pan, Y. (2016). The pseudo-Thellier palaeointensity method: New calibration and uncertainty estimates. *Geophysical Journal International*, *207*(3), 1596–1608. https://doi.org/10.1093/gji/ggw349

Paterson, G. A., Muxworthy, A. R., Yamamoto, Y., & Pan, Y. (2017). Bulk magnetic domain stability controls paleointensity fidelity. *Proceedings of the National Academy of Sciences of the United States of America*, *114*(50), 13120–13125. https://doi.org/10.1073/pnas.1714047114

Paterson, G. A., Tauxe, L., Biggin, A. J., Shaar, R., & Jonestrask, L. C. (2014). *Standard paleointensity definitions v1.1, 0–43*. Retrieved from http://www.paleomag.net/SPD/spdweb.html

Riisager, P., & Riisager, J. (2001). Detecting multidomain magnetic grains in Thellier palaeointensity experiments. *Physics of the Earth and Planetary Interiors*, *125*(1–4), 111–117. https://doi.org/10.1016/S0031-9201(01)00236-9

Schmidt, P. W. (1993). Palaeomagnetic cleaning strategies. *Physics of the Earth and Planetary Interiors*, *76*(1–2), 169–178. https://doi.org/10.1016/0031-9201(93)90066-I

Selkin, P. A., Gee, J. S., Tauxe, L., Meurer, W. P., & Newell, A. J. (2000). The effect of remanence anisotropy on paleointensity estimates: A case study from the Archean Stillwater Complex. *Earth and Planetary Science Letters*, *183*(3–4), 403–416. https://doi.org/10.1016/S0012-821X(00)00292-2

Shaar, R., & Tauxe, L. (2013). Thellier GUI: An integrated tool for analyzing paleointensity data from Thellier-type experiments. *Geochemistry, Geophysics, Geosystems*, *14*, 677–692. https://doi.org/10.1002/ggge.20062

Shaar, R., & Tauxe, L. (2015). Instability of thermoremanence and the problem of estimating the ancient geomagnetic field strength from non-single-domain recorders. *Proceedings of the National Academy of Sciences of the United States of America*, *112*(36), 11187–11192. https://doi.org/10.1073/pnas.1507986112

Shcherbakov, V. P., Gribov, S. K., Lhuillier, F., Aphinogenova, N. A., & Tsel'movich, V. A. (2019). On the reliability of absolute palaeointensity determinations on vasaltic rocks bearing a thermochemical remanence. *Journal of Geophysical Research: Solid Earth*, *124*(8), 7616–7632. https://doi.org/10.1029/2019JB017873

Smirnov, A. V. (2017). Intensity of geomagnetic field in the Precambrian and evolution of the Earth's deep interior. *Izvestiya, Physics of the Solid Earth*, *53*(5), 760–768. https://doi.org/10.1134/S1069351317050123

Smirnov, A. V., Kulakov, E. V., Foucher, M. S., & Bristol, K. E. (2017). Intrinsic paleointensity bias and the long-term history of the geodynamo. *Science Advances*, *3*(2), 1–8. https://doi.org/10.1126/sciadv.1602306

Smirnov, A. V., & Tarduno, J. A. (2005). Thermochemical remanent magnetization in Precambrian rocks: Are we sure the geomagnetic field was weak? *Journal of Geophysical Research*, *110*(6). https://doi.org/10.1029/2004JB003445

Smirnov, A. V., Tarduno, J. A., & Evans, D. A. D. (2011). Evolving core conditions ca. 2 billion years ago detected by paleosecular variation. *Physics of the Earth and Planetary Interiors*, *187*(3–4), 225–231. https://doi.org/10.1016/j.pepi.2011.05.003

Sprain, C. J., Swanson-Hysell, N. L., Fairchild, L. M., & Gaastra, K. (2018). A field like today's? The strength of the geomagnetic field 1.1 billion years ago. *Geophysical Journal International*, *213*(3), 1969–1983. https://doi.org/10.1093/gji/ggy074

Suttie, N., Shaw, J., & Hill, M. J. (2010). Direct demonstration of microwave demagnetization of a whole rock sample with minimal heating. *Earth and Planetary Science Letters*, *292*, 357–362. https://doi.org/10.1016/j.epsl.2010.02.002

Tanaka, H., & Komuro, N. (2009). The Shaw paleointensity method: Can the ARM simulate the TRM alteration? *Physics of the Earth and Planetary Interiors*, *173*(3–4), 269–278. https://doi.org/10.1016/j.pepi.2009.01.003

Tarduno, J. A., Cottrell, R. D., Bono, R. K., Oda, H., Davis, W. J., Fayek, M., et al. (2020). Paleomagnetism indicates that primary magnetite in zircon records a strong Hadean geodynamo. *Proceedings of the National Academy of Sciences of the United States of America*, *117*(5), 2309–2318. https://doi.org/10.1073/pnas.1916553117

Tauxe, L., Santos, C. N., Cych, B., Zhao, X., Roberts, A. P., Nagy, L., & Williams, W. (2021). Understanding nonideal paleointensity recording in igneous rocks: Insights from aging experiments on lava samples and the causes and consequences of "fragile" curvature in Arai plots. *Geochemistry, Geophysics, Geosystems*, *22*(1), 1–24. https://doi.org/10.1029/2020GC009423

Tauxe, L., & Staudigel, H. (2004). Strength of the geomagnetic field in the cretaceous normal superchron: New data from submarine basaltic glass of the troodos ophiolite. *Geochemistry, Geophysics, Geosystems*, *5*(2). https://doi.org/10.1029/2003GC000635

Tsunakawa, H., & Shaw, J. (1994). The Shaw method of palaeointensity determinations and its application to recent volcanic rocks. *Geophysical Journal International*, *118*(3), 781–787. https://doi.org/10.1111/j.1365-246X.1994.tb03999.x

Valet, J. P., Brassart, J., Le Meur, I., Soler, V., Quidelleur, X., Tric, E., & Gillot, P. Y. (1996). Absolute paleointensity and magnetomineralogical changes. *Journal of Geophysical Research*, *101*, 25029–25044. https://doi.org/10.1029/96jb02115

Walton, D., Shaw, J., Share, J., & Hakes, J. (1992). Microwave demagnetization. *Journal of Applied Physics*, *71*(3), 1549–1551. https://doi.org/10.1063/1.351230

Wilson, R. L., & Watkins, N. D. (1967). Correlation of petrology and natural magnetic polarity in Columbia Plateau basalts. *Geophysical Journal of the Royal Astronomical Society*, *12*(4), 405–424. https://doi.org/10.1111/j.1365-246X.1967.tb03150.x

Wingate, M. T. D., & Giddings, J. W. (2000). Age and palaeomagnetism of the Mundine Well dyke swarm, Western Australia: Implications for an Australia-Laurentia connection at 755 Ma. *Precambrian Research*, *100*(1–3), 335–357. https://doi.org/10.1016/S0301-9268(99)00080-7

Wingate, M. T. D., Pisarevsky, S. A., & Evans, D. A. D. (2002). Rodinia connections between Australia and Laurentia: No SWEAT, no AUSWUS? *Terra Nova*, *14*(2), 121–128. https://doi.org/10.1046/j.1365-3121.2002.00401.x

Yamamoto, Y., Tsunakawa, H., Shaw, J., & Kono, M. (2007). Paleomagnetism of the Datong monogenetic volcanoes in China: Paleodirection and paleointensity during the middle to early Brunhes Chron. *Earth, Planets and Space*, *59*(7), 727–746. https://doi.org/10.1186/BF03352736

Yamamoto, Y., Tsunakawa, H., & Shibuya, H. (2003). Palaeointensity study of the Hawaiian 1960 lava: Implications for possible causes of erroneously high intensities. *Geophysical Journal International*, *153*(1), 263–276. https://doi.org/10.1046/j.1365-246X.2003.01909.x

Yamamoto, Y., & Yamaoka, R. (2018). Paleointensity study on the holocene surface lavas on the island of Hawaii using the Tsunakawa–Shaw method. *Frontiers in Earth Science*, *6*, 1–10. https://doi.org/10.3389/feart.2018.00048

Yu, Y., & Tauxe, L. (2005). Testing the IZZI protocol of geomagnetic field intensity determination. *Geochemistry, Geophysics, Geosystems*, *6*(5). https://doi.org/10.1029/2004GC000840